

1 **Long-range transport of Asian dust to the Arctic:**
2 **identification of transport pathways, evolution of**
3 **aerosol optical properties, and impact assessment on**
4 **surface albedo changes**

5
6 **Xiaoxi Zhao¹, Kan Huang^{1,3,4*}, Joshua S. Fu², Sabur F. Abdullaev⁵**

7 ¹Center for Atmospheric Chemistry Study, Shanghai Key Laboratory of Atmospheric Particle
8 Pollution and Prevention (LAP³), Department of Environmental Science and Engineering, Fudan
9 University, Shanghai, 200433, China

10 ²Department of Civil and Environmental Engineering, University of Tennessee, Knoxville, TN,
11 USA

12 ³IRDR ICoE on Risk Interconnectivity and Governance on Weather/Climate Extremes Impact and
13 Public Health, Fudan University, Shanghai 200433, China

14 ⁴Institute of Eco-Chongming (IEC), Shanghai, 202162, China

15 ⁵Physical Technical Institute of the Academy of Sciences of Tajikistan, Dushanbe, Tajikistan

16 **Corresponding author:** huangkan@fudan.edu.cn

17
18 **Abstract**

19 Airborne dust is one of the most important natural aerosols, it has various
20 environmental impacts on air quality, ocean fertilization, and the global climate change.

21 Asian dust, representing one of the major dust sources in the world, has been widely
22 studied due to its long-range transport capability. However, its transport to the Arctic
23 has been less investigated. In this study, two typical transport routes were identified
24 based on the recorded dust events in China during 2011-2015. Accordingly, two specific

25 Asian dust long-range transport events were selected and compared, i.e., one observed
26 at Barrow, Alaska (travelled mostly over lands within 6-7 days) and the other one
27 observed at Alert, Canada (travelled mostly over oceans within 7-8 days). The transport
28 routes of the two dust events had been cross-validated by using air mass trajectory
29 modeling, meteorology reanalysis data, ground-based aerosol columnar and profiling
30 observations, and spaceborne remote sensing. It was found that different transport
31 routes to the Arctic had divergent effects on the evolution of aerosol properties,
32 revealing different mixing extents between dust, anthropogenic particles, smoke, and
33 sea salts. Based on the SNow ICe Aerosol Radiative model, the albedo simulation
34 indicated that dust and elemental carbon together reduced the surface albedo by 0.35%
35 to 2.63% compared to the pure snow condition. This study implied that the dust long-
36 transport from China to the Arctic was ubiquitous and may be a potential contributor to
37 the Arctic regional climate ~~and ecosystem~~.

38

39 **1. Introduction**

40 In the context of global warming, the Arctic temperature has been increasing at a rate
41 higher than the global average in recent decades, which is the so-called “Arctic
42 Amplification” effect (Serreze et al., 2009; Serreze and Francis, 2006). Although the
43 increase of greenhouse gases concentrations was an important driver of the Arctic and
44 global warming, the underlying cause of Arctic amplification remained uncertain as
45 Arctic warming and ice cap melting were also associated with changes in surface albedo,
46 aerosol radiative forcing, cloud cover, atmospheric water vapor content, seawater

47 temperature, and etc. (Screen and Simmonds, 2010; Gillett et al., 2008). The
48 magnitudes of direct radiative forcing of Arctic aerosols were closely related to the
49 origin of aerosols, and its transport, and deposition (Quinn et al., 2008). During the long
50 transport of aerosols to the Arctic, the solar radiation could be absorbed or scattered by
51 some components in the aerosols (black carbon, sulfate, etc.), which led to a decrease
52 of the amount of solar radiation reaching the surface. However, this cooling effect may
53 be diminished by the decrease of Arctic aerosol concentrations in recent decades
54 (Gagne et al., 2017; Breider et al., 2017). On the other hand, aerosol-radiation
55 interactions also contributed to Arctic warming in the following ways. Firstly,
56 absorbing aerosols at low latitudes could enhance the latitudinal gradient of temperature,
57 thus enhancing heat transport from other regions to the Arctic (Sand et al., 2013b; Sand
58 et al., 2013a); Secondly, absorbing aerosols absorbed solar radiation and warmed the
59 Arctic atmosphere while the surface was cooled, which enhanced atmospheric stability
60 and constrained the diffusion of air pollutants (Blanchet and List, 2010; Koch and Del
61 Genio, 2010; Brock et al., 2011); Thirdly, deposition of absorbing aerosols onto snow
62 and ice could reduce the surface albedo of the Arctic and thus led to local warming.
63 Besides, the formation of mixed-phase clouds in the Arctic were found related to low
64 concentrations and acid coating of dust particles based on both global and parcel model
65 simulations (Fan, 2013). Overall, direct and indirect radiative forcings caused by
66 aerosols had significant impacts on the Arctic climate as demonstrated by the model
67 simulation results (Shindell and Faluvegi, 2009; Flanner, 2013). In addition to the
68 impact of absorbing aerosols on the Arctic climate, the snow-albedo feedback and

69 cloud-albedo feedback in Central Siberia significantly regulated the variation of dust
70 emissions in spring over the Gobi Desert (Liu et al., 2018).

71 Due to the sparse human activities in the Arctic, most of the air pollutants
72 originated from the middle and lower latitudes, e.g., Eurasia, Siberia, North America,
73 and Southeast Asia. Eurasia was the main source area for the lower Arctic altitudes and
74 the higher Arctic altitudes was mainly influenced by South and Central Asia (Qi et al.,
75 2017; Fisher et al., 2011; Sharma et al., 2013; Stohl, 2006). Di Pierro et al. (2011) and
76 Huang et al. (2015a) both used ground-based lidar data and satellite remote sensing
77 images to demonstrate that aerosols from China can be transported to the Arctic within
78 4-6 days. Similarly, Di Biagio et al. (2018) found that aerosols in the high Arctic north
79 of Svalbard from October, 2014 to June, 2015 were mainly from Russia. Warneke et al.
80 (2010) found that forest fires in Russia strongly affected air pollutant concentrations in
81 the Arctic atmosphere and surface snowpack based on aircraft observations and
82 numerical simulation. Marelle et al. (2015) investigated a long-transport event from
83 Europe to the Arctic in April, 2008 and estimated a maximum shortwave radiation of
84 3.3 W m^{-2} at the top of the atmosphere, yielding a significant local warming effect.
85 Sobhani et al. (2018) applied the WRF-STEM (Weather Research and Forecasting -
86 sulfur transport and deposition model) model to study the long-range transport of
87 aerosols to the Arctic and calculated the contribution of various anthropogenic and
88 biomass burning emissions. Europe and China were found as the main source regions
89 of Arctic black carbon, contributing about 46% and 25% in the middle and upper
90 troposphere, respectively.

91 Different from black carbon, dust had a much larger geographic influencing
92 coverage due to that dust particles were usually accompanied with strong winds.
93 Although a number of studies focused on local or regional dust in the Arctic (Ferrero et
94 al., 2019; Ranjbar et al., 2021; Dagsson-Waldhauserova et al., 2019), the long-range
95 transport of dust to the Arctic has been frequently observed. Asian dust can be
96 transported across the Pacific Ocean to reach North America and even the Arctic (Wang
97 et al., 2018b; Guo et al., 2017). Zwaafink et al. (2016) combined a Lagrangian particle
98 dispersion model FLEXPART (FLEXible PARTicle dispersion model) and surface
99 particle concentration observations to simulate the global dust emissions. It was
100 ~~estimated that the dust loading in the Arctic was dominated by Asia (38%) and Africa~~
101 ~~(32%) sources while the local contribution was around 27%. found that t~~The
102 instantaneous radiative forcing in the Arctic caused by dust was also dominated by Asia
103 and Africa. In addition, the deposition of dust on snow was responsible for almost all
104 ~~of the bottom of the atmosphere~~ instantaneous radiative forcing at the bottom of the
105 atmosphere (Kylling et al., 2018).

106 Although both observational and modeling studies showed a persistent source of
107 the Arctic dust from Asia (Fan, 2013; Ginoux et al., 2012), the transport pathways were
108 seldom explored. Huang et al. (2015b) revealed an unreported transport path of Asian
109 dust to the Arctic and estimated its transport duration. In this study, the frequency of
110 dust from ~~China~~ East Asia that had the capability to be transported to the Arctic was
111 estimated. Two typical dust transport pathways to the Arctic were investigated based on
112 a synergy of remote sensing data and Arctic monitoring data. The evolutions of aerosol

113 optical properties during the long-range transport were analyzed. Finally, the potential
114 impact of absorbing aerosol on the decrease of surface albedo was quantified.

115

116 **2. Data and Methodology**

117 **2.1. Receptor sites in the Arctic**

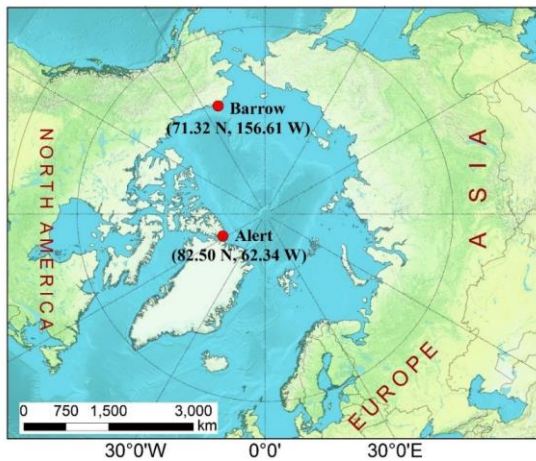
118 Two Arctic monitoring sites were chosen as the investigated receptors (Figure 1).—

119 They are almost the most northern sites in the Arctic Circle and located in the remote
120 regions where human activities are negligible. Thus, the long-range transported
121 particles can be easily discerned. One site is Barrow (71.32°N, 156.61°W) located in

122 the northernmost part of the Alaska region of USA. It is surrounded by the Arctic
123 Ocean on three sides and has a large ice cap. Barrow is characterized of a cold and dry
124 climate and covered by snow and ice all year round with an average annual
125 temperature of about -11°C (Dong et al., 2010). In winter, the frequency of northerly
126 air currents was high. The average surface temperature reached as low as -25°C in
127 January and February and most of the snowfall occurred at the end of February. Since
128 April, the invasion of warm and moist air masses from the North Pacific Ocean began
129 to prompt the snowpack in Alaska to melt (Stone et al., 2002). This site is managed by
130 Earth System Research Laboratory of National Oceanic and Atmospheric
131 Administration.

132 The other site is Alert (82.50°N, 62.34°W) in the Nunavut region of Canada, the
133 northernmost permanent human settlement in the world. This site is located about 500
134 km north of Greenland, near the North Pole and far from any industrial emissions. It

135 is very cold due to the long-lasting polar night with four months in a year. The
136 average temperature was below -30°C from December to March and the average
137 annual temperature was -17.9°C (Weijers et al., 2017). This site is managed by
138 Environment Canada.



139
140 Figure 1. Two receptor sites (Barrow and Alert) in the Arctic. The map is created by
141 ArcGIS 10.2.

143 2.2. Aerosol measurements

144 Particles at Barrow and Alert were measured by the three-wavelength (450, 550, and
145 700nm) Integrating Nephelometer (Model 3563). The nephelometer measured the
146 angular integral of light scattering and Beer-Lambert Law was applied to calculate the
147 light extinction. In this study, the measurement results at 550nm were used. Aerosol
148 absorption was measured by a filter absorption photometer. The aerosol absorption
149 coefficients were obtained at three wavelengths of 467, 530, and 660nm. The
150 measurement results at 530nm were used. Aerosol Robotic Network (AERONET)

Formatted: Font color: Auto

Formatted: Font color: Auto

Formatted: Font: (Asian) +Body Asian (等线), Font color: Auto

151 established a global observational network of columnar aerosol optical properties
152 based on Cimel-31 Sun Photometers (Holben et al., 1998). Key parameters of aerosol
153 optical properties were retrieved at 440 nm, 670 nm, 870 nm, and 1020 nm,
154 respectively. The quality-assured level 2.0 data were used. The AD-Net (Asian dust
155 and aerosol lidar observation network) operated by National Institute for
156 Environmental Studies (NIES) established a lidar network of dual-wavelength
157 depolarization lidars (Model: L2S-SM II), aiming to obtain the four dimensional
158 distributions (sites/time/height/aerosol properties) of aerosol particles in East Asia
159 (Shimizu et al., 2017). The lidar could measure backscattering coefficients and the
160 depolarization ratio at the wavelength of 532 nm. The lidar continuously operated
161 with 15 min intervals and 30m ~~vertical height~~ resolution.

162 In addition to the ground-based sites, remote sensing from space was used to
163 provide widespread spatial information of aerosols. The MODIS (Moderate-resolution
164 Imaging Spectroradiometer) Level-3 aerosol products ($1^\circ \times 1^\circ$) were obtained from
165 NASA's Giovanni (<https://giovanni.gsfc.nasa.gov/giovanni/>). Aerosol optical depth
166 (550nm) data was based on the Dark Target ([Levy et al., 2007](#)) and Deep Blue ([Hsu et](#)
167 [al., 2013](#)) algorithm and Angström exponent (0.412-0.47nm) data was based on the
168 Deep Blue algorithm. The CALIOP (Cloud-Aerosol Lidar with Orthogonal
169 Polarization) Lidar onboard the CALIPSO (Cloud-Aerosol Lidar and Infrared
170 Pathfinder Satellite Observation) satellite provided global data on aerosol and cloud
171 layers with a horizontal and vertical resolution of around 5km and 60m. Track scale
172 vertical aerosol profiles were derived. In addition, major aerosol subtypes can be

173 identified, including dust, smoke, clean continental, polluted continental, clean
174 marine, and polluted dust ([Omar et al., 2009](#)).

175

176 **2.3. Air mass trajectories modeling**

177 To track the possible source regions of airborne particles, HYSPLIT4 (HYbrid Single-
178 Particle Lagrangian Integrated Trajectory) was run online at the NOAA (National
179 Oceanic and Atmospheric Administration) ARL (Air Resource
180 Laboratory) READY (Real-time Environmental Applications and Display sYstem)
181 Website (<http://www.arl.noaa.gov/ready/hysplit4.html>). The HYSPLIT model is a
182 complete system for calculating simple air mass backward trajectories, in addition to
183 dispersion and complex deposition simulations (Draxier and Hess, 1998). The
184 meteorological input data used in the model were obtained from the National Center
185 for Environmental Prediction's (NCEP) global data assimilation system (GDAS) with
186 a horizontal resolution of $0.5^\circ \times 0.5^\circ$.

187

188 **2.4. Snow albedo modeling**

189 The Snow–Ice–Aerosol–Radiative (SNICAR) model was used to simulate the impact
190 of impurity (e.g. dust, black carbon, and volcanic ash) on the surface albedo of snow
191 and ice (Flanner et al., 2007). The application of the SNICAR model required inputs
192 such as snow grain effective radius, snowpack thickness/density, surface albedo, the
193 concentrations of impurities in snow. The effective grain sizes of snow ranged from
194 $100 \mu\text{m}$ for fresh clean snow to $1500 \mu\text{m}$ for aged snow and granular ice. Table 1 lists

195 the parameters considered for SNICAR in this study. The parameters of snow were
 196 derived from field measurements at Barrow in April, 2015 (Dou et al., 2017) and near
 197 Alert in February and April, 2000 (Domine et al., 2002). The estimation of impurities
 198 concentrations in snow will be presented in Section 3.7.1.

199

200 **Table 1. The input parameters in the SNICAR model**

Parameters	Barrow	Alert
Incident radiation		Direct
Surface spectral distribution		Summit Greenland, clear-sky
Snow grain effective radius (μm)	180(Dou et al., 2017)	500 (0.1-1.5mm)(Domine et al., 2002)
Snowpack thickness (m)	0.35(Dou et al., 2017)	0.4(Domine et al., 2002)
Snowpack density (kg/m^3)	350(Dou et al., 2017)	300(Domine et al., 2002)
Albedo of underlying ground	0.73 (300-700nm)	0.33 (700-5000nm) (Dou et al., 2017)

201

202 3. Results and Discussion

203 3.1. Overview of dust events in China from 2011-2015

204 Table 2 summarizes the occurrence frequency and duration of dust events in the dust
 205 source regions of China during 2011-2015 recorded by China's Sand-dust Weather
 206 Almanac (Cma, 2013, 2014, 2015, 2016, 2017). A total of 50 dust events occurred,
 207 which were categorized into three types, i.e., floating dust, dust storm, and severe dust
 208 storm. Among them, the occurrence frequency of floating dust reached 36, accounting
 209 for 72% of the total dust events. On average, floating dust occurred about 7 times a year
 210 with a total duration of 61 days. The occurrence frequencies of dust storm and severe
 211 dust storm events were both 7 times with the total duration of 18 days. Compared with

212 2000-2010, the frequency of dust storm and severe dust storm events during the last
213 five years decreased significantly, while that of floating dust increased.

214

215 **Table 2. Summary of dust weather conditions in China during 2011 – 2015**

216

Year	floating dust		dust storm		severe dust storm		Total frequency
	frequency	days	frequency	days	frequency	days	
2011	5	10	1	3	2	6	8
2012	5	10	3	8	2	4	10
2013	9	15	1	2			10
2014	4	8	1	2	2	6	7
2015	13	18	1	3	1	2	15
Total	36	61	7	18	7	18	50

217

218 On a seasonal basis (Table 3), the springtime (March-May) was the peak period of
219 dust outbreak in China. 41 dust events occurred, accounting for 82% of the total dust
220 events. Of which, relatively high frequencies of dust storm and severe dust storm events
221 were observed, accounting for 37.5% of the total events in April. This high frequency
222 of dust occurrence in the spring of China was mainly related to the climatic
223 characteristics, geographic conditions, and geological structure of northern China.
224 Strong winds caused by the Inner Mongolia cyclone and cold fronts in spring resulted
225 in the frequent outbreak of dusty weather in northern China. In terms of the
226 geographical dust source areas in China, the source regions of dust included the South
227 Xinjiang basin, central and western Inner Mongolia, central and western Gansu, and
228 northern Shaanxi.

229

230 **Table 3. Monthly summary of dust days in China during 2011 – 2015**

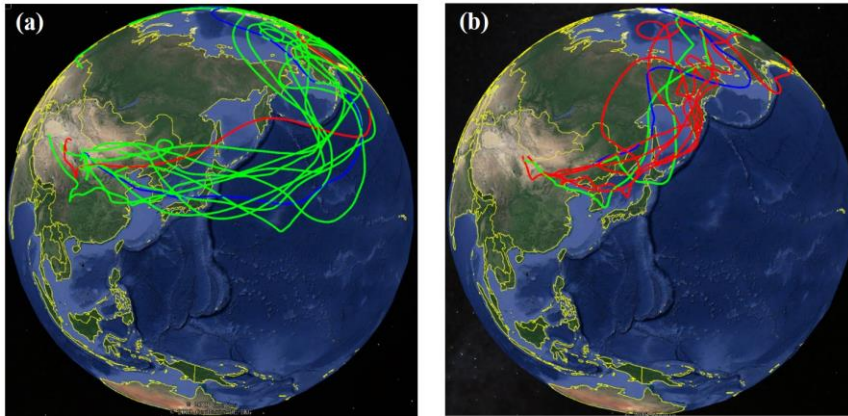
Month	floating dust	dust storm	severe dust storm	total
February	3			3
March	12	1	2	15
April	10	3	3	16
May	7	1	2	10
June	1			1
August	1			1
November	2	2		4

231

232 **3.2 Transport pathways of Asian dust to the Arctic**

233 In order to investigate the frequency and transport pathways of dust from China to the
234 Arctic, the HYSPLIT trajectory model was applied in this study. Based on the outbreak
235 time and source areas of dust recorded by China's Sand-dust Weather Almanac, 10-15
236 days forward trajectories starting at typical altitudes of lifted dust (500m, 1000m, and
237 1500m) were computed for each dust event in China during 2011-2015. If the
238 trajectories entered the Arctic Circle (latitudes higher than 66°34'N), the specific dust
239 event was recorded as one dust long-range transport event from China to the Arctic.

240



241

242

243

244

245

246

247

248

Figure 2. Two common transport pathways of dust originating from China to the Arctic, i.e., (a) the northern China - Korean Peninsula/Japan - North Pacific Ocean – Arctic pathway and (b) the northern China - Korean Peninsula/Japan - Kamchatka Peninsula - East Siberia – Arctic pathway. Red, blue, and green curves represent forward trajectories starting at altitudes of 500m, 1000m, and 1500, respectively. The map is © Google Earth 2019.

249

250

251

252

253

254

255

256

257

258

259

Based on this criterion, 38 out of the 50 dust events that originated from China during 2011-2015 had the potential migrating to the Arctic Circle. Among these identified dust events, most occurred in spring with 32 events and the transport duration varied between 4 and 13 days. Two main types of dust transport from China to the Arctic were distinguished in Figure 2. As for Type I (Figure 2a), dust mainly originated from the central parts of Inner Mongolia and central Gansu. It passed through northern China, Korean Peninsula, Japan and the North Pacific Ocean, and finally reached Siberia and the northern part of Alaska. This transport type was characterized of wide geographic coverage, relatively long transport duration (about 7-10 days), and mainly over the open ocean. This was due to the high lifting altitude (mostly over 1500m) over the dust source regions, so particles can be transported to even further areas.

260 As for Type II (Figure 2b), dust mainly originated from northeast China and
261 western Inner Mongolia, then passing over the Korean Peninsula, northern Japan,
262 Kamchatka Peninsula, and finally reaching East Siberia and its northern areas.
263 Compared to Type I, the Type II transport pathways travelled more over land and had
264 relatively shorter duration of about 4-8 days. This was due to the presence of a low-
265 pressure system over northern Japan in spring, which induced the air masses deflecting
266 northward. In Section 3.4, more details about the low-pressure system will be presented
267 based on case analysis. More explicit characterizations of the transport pathways from
268 the dust source regions to the Arctic will be discussed later in Section 3.5.

Formatted: Font color: Auto

Formatted: Font color: Auto

Formatted: Font color: Auto

Formatted: Font color: Auto

Formatted: Font color: Auto

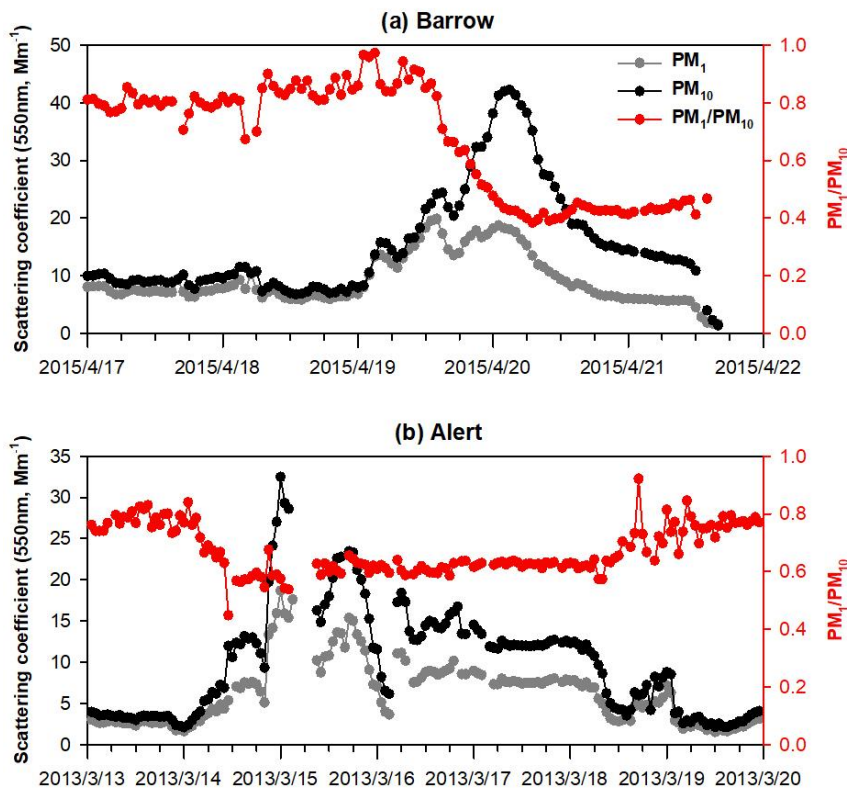
269

270 3.3 Two cases of long-range transported dust to the Arctic

271 Figure 3a shows the time series of scattering coefficients (σ_{sp}) of PM_1 and PM_{10} at 550
272 nm at Barrow during April 17-21, 2015. The scattering coefficients stayed at low levels
273 from the early morning of April 17 to the evening of April 18, which were similar to
274 the annual average values at Barrow in 2015 ($4.8 Mm^{-1}$ and $8.1 Mm^{-1}$ for PM_1 and PM_{10} ,
275 respectively). Since the early morning of April 19, both $\sigma_{sp}(PM_1)$ and $\sigma_{sp}(PM_{10})$
276 climbed simultaneously, indicating the invasion of air pollutants. At 15:00 on April 19,
277 $\sigma_{sp}(PM_1)$ reached relatively high value of $19.8 Mm^{-1}$ and was still close to that of PM_{10}
278 with the $\sigma_{sp}(PM_1)/\sigma_{sp}(PM_{10})$ ratio of 0.82, indicating fine particles dominated during
279 this period. Afterwards, $\sigma_{sp}(PM_{10})$ continued to increase until it reached the maximum
280 value of $42.2 Mm^{-1}$ at 4:00 on April 20, more than 5 times of its annual average. The
281 mean $\sigma_{sp}(PM_1)/\sigma_{sp}(PM_{10})$ ratio during 14:00, April 19 - 12:00, April 21 decreased to

282 0.47 ± 0.10 , obviously indicating the enrichment of coarse particles. This episode is
283 defined as CASE I.

284 Figure 3b shows the time series of scattering coefficients of PM_{10} and PM_{10} at 550
285 nm at Alert from March 13 to 19, 2013. The annual average $\sigma_{sp}(PM_{10})$ and $\sigma_{sp}(PM_{10})$
286 at Alert was $4.2 Mm^{-1}$ and $6.0 Mm^{-1}$, respectively, slightly lower than those observed at
287 Barrow. From 0:00 on March 14, $\sigma_{sp}(PM_{10})$ and $\sigma_{sp}(PM_{10})$ started to increase and
288 reached the maximum values of $18.6 Mm^{-1}$ and $32.3 Mm^{-1}$ at 0:00 on March 15, which
289 were more than 4 and 5 times of their annual average, respectively. The mean $\sigma_{sp}(PM_{10})/$
290 $\sigma_{sp}(PM_{10})$ ratio during 11:00 ~~on~~ March 14 to 7:00 on March 18 was 0.61 ± 0.03 , also
291 indicating the enrichment of coarse particles. This episode is defined as CASE II.



292
 293 **Figure 3. (a) Time series of hourly scattering coefficients of PM₁ and PM₁₀ at 550**
 294 **nm and the ratio of PM₁/PM₁₀ at Barrow during April 17-21, 2015. (b) The same**
 295 **but for Alert during March 13 to 19, 2013.**

296

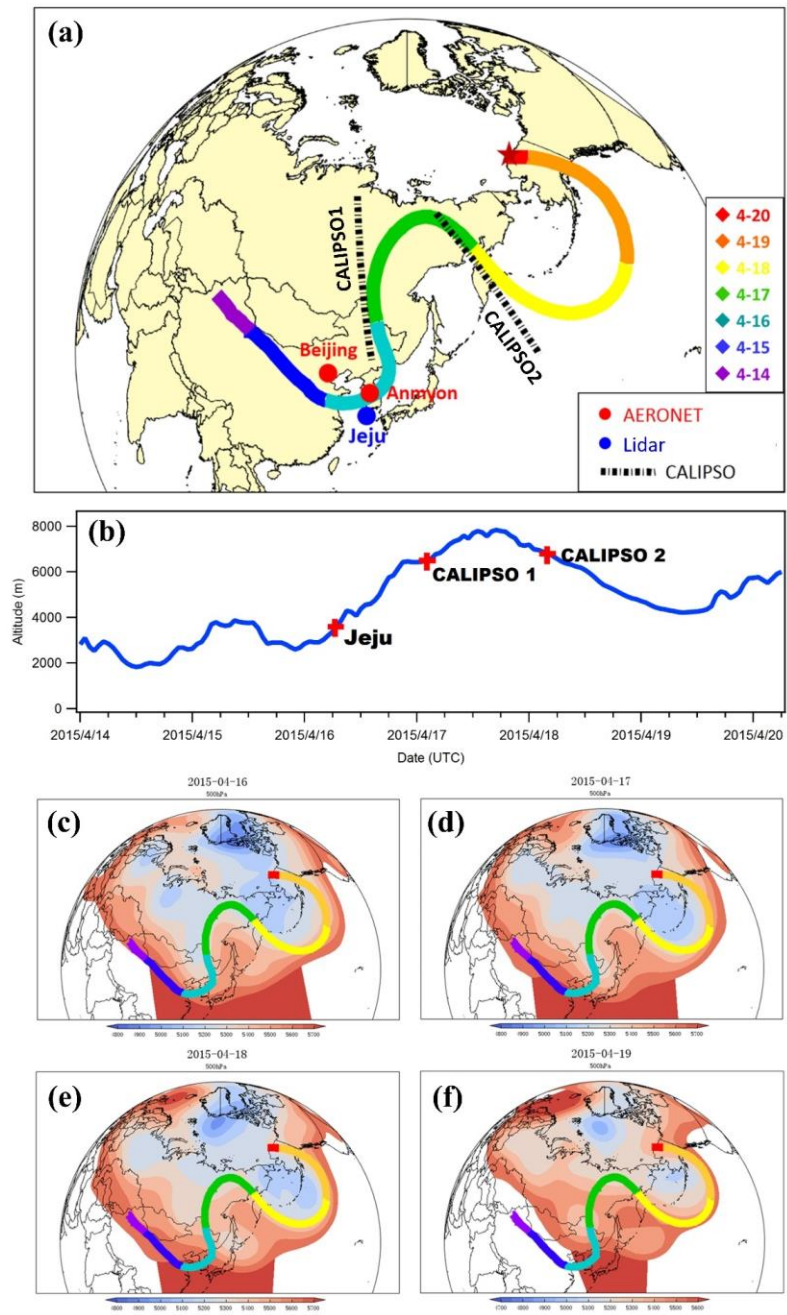
297 In comparison, the pollution during CASE I lasted for a relatively short period of
 298 about 2.5 days while had higher peak values of $\sigma_{sp}(PM_{10})$ than CASE II, indicating that
 299 CASE I was subject to stronger long-range transport and more significant variations of
 300 synoptic conditions. The pollution during CASE II lasted for nearly four days,
 301 suggesting relatively weak cleanup processes of the air pollutants. As for the $\sigma_{sp}(PM_1)/$
 302 $\sigma_{sp}(PM_{10})$ ratio, it was much lower in CASE I than that in CASE II. This indicated the
 303 intrusion of coarse particles was more intense during CASE I, which could be related

304 to various factors such as the emission source regions, transport pathways, and
305 evolution of particles. In the next section, the transport pathways of the two cases above
306 were validated by using backward trajectory analysis and remote sensing from both
307 space and ground-based observations.

308

309 **3.4 Identification of dust long-range transport pathways**

310 To determine the sources and transport pathways of the two Arctic pollution events, the
311 HYSPLIT model was applied to compute the air masses transport trajectories. Figure
312 4a shows the 7-days backward trajectory simulated at an altitude of 6 km above Barrow
313 starting from 04:00 on April 20, 2015 (CASE I). The different segments of the trajectory
314 were colored to represent the continuous dates. On 14-15 April, air masses originated
315 from the Taklamakan and Gobi deserts in China, then passed over East Asia, Siberia of
316 Russia, and the Pacific Ocean, and finally reached Barrow about 6 days later. The
317 geopotential height fields based on the NCEP reanalysis data are plotted in Figure 4c-
318 4f to verify the dust transport path. On April 16, a low-pressure trough over Northeast
319 China caused the eastward air masses to turn northward. On April 17, the air masses
320 followed the high-pressure ridge over eastern Russia and entered the North Pacific.
321 Then its direction was again deflected by a low-pressure system near the Bering Strait
322 on April 18 and 19, finally reaching Barrow on April 20.



323

324

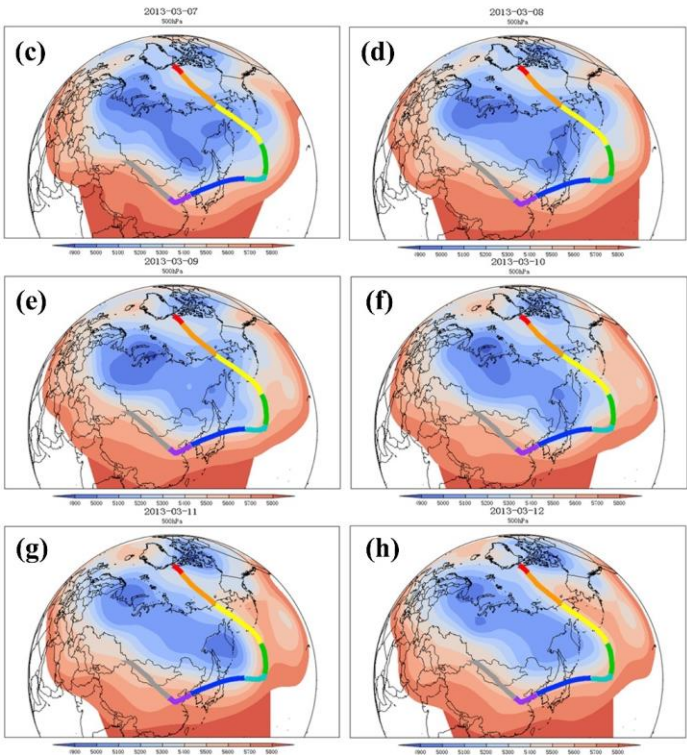
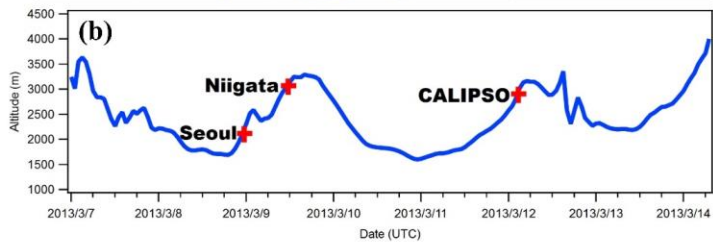
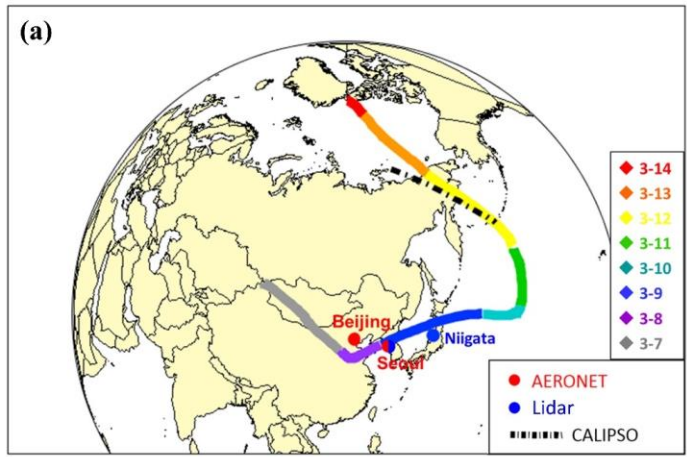
325 **Figure 4. (a) The 7-days backward trajectory simulated at an altitude of 6 km**

326 **above Barrow starting from 04:00 on April 20, 2015. The locations of AERONET,**
327 **Lidar sites, and CALIPSO tracks nearby the trajectory are plotted. (b) The height**
328 **of the trajectory along the transport path. The height and time of dust layers**
329 **observed by lidars and CALIPSO in Figure 4a are indicated by the red plus**
330 **symbols. (c-f) Daily geopotential height fields (500 hPa) from the NCEP reanalysis**
331 **data**

332

333 Figure 5a shows a typical backward trajectory simulated at an altitude of 4 km
334 above Alert on March 14, 2013 (CASE II). On March 7, air masses travelled over the
335 Gobi Desert on the border between Mongolia and the north of China, then passed over
336 Korea and Japan, and directly entered the Pacific Ocean. Afterwards, it kept moving
337 northward across the Arctic Ocean and reached Alert on March 14. Based on the
338 geopotential heights (Figure 5c-5h), a low-pressure system was observed over the
339 eastern coast of Russia and kept moving to the southeast from March 7 to 11. On March
340 11, the low-pressure system moved over the Sea of Okhotsk in Russia and turned to be
341 stronger, causing the air masses deflect and follow the geopotential height contours all
342 the way north to Alert.

343



345 **Figure 5. Same as Figure 4 but for CASE II.**

346

347 **3.5 Verification of dust transport pathways based on satellite and ground-based**
348 **observations**

349 Although the air mass transport pathways of the two Arctic coarse particle pollution
350 cases were visualized based on trajectory modeling, whether dust particles were indeed
351 present in the air masses has not been confirmed. In this section, the aerosol optical
352 properties along the transport pathway were explored using both ground-based
353 observations (AERONET and AD-Net) and satellite inversion data (CALIPSO). In
354 Figure 4a and 5a, the red dots denoted the AERONET sites, which observed columnar
355 aerosol optical properties. The blue dots denoted the AD-Net sites, which observed
356 vertical profiles of aerosol extinctions and particle ~~morphology_spheric~~ information.
357 The black dashed lines represented the orbits of CALIPSO profiles, which were used
358 to supplement the aerosol information in the blank areas without available ground-
359 based observations. The validation results of the two cases are described separately as
360 below.

361

362 **(i) CASE I**

363 Figures 6 shows the aerosol optical properties of two AERONET sites, i.e., Beijing
364 (China) and Anmyon (Korea), which were located nearby the air mass transport
365 pathway in CASE I (Figure 4a). AE (Angström exponent) is a parameter of
366 characterizing the particle size. The smaller AE represents the larger particle size, and

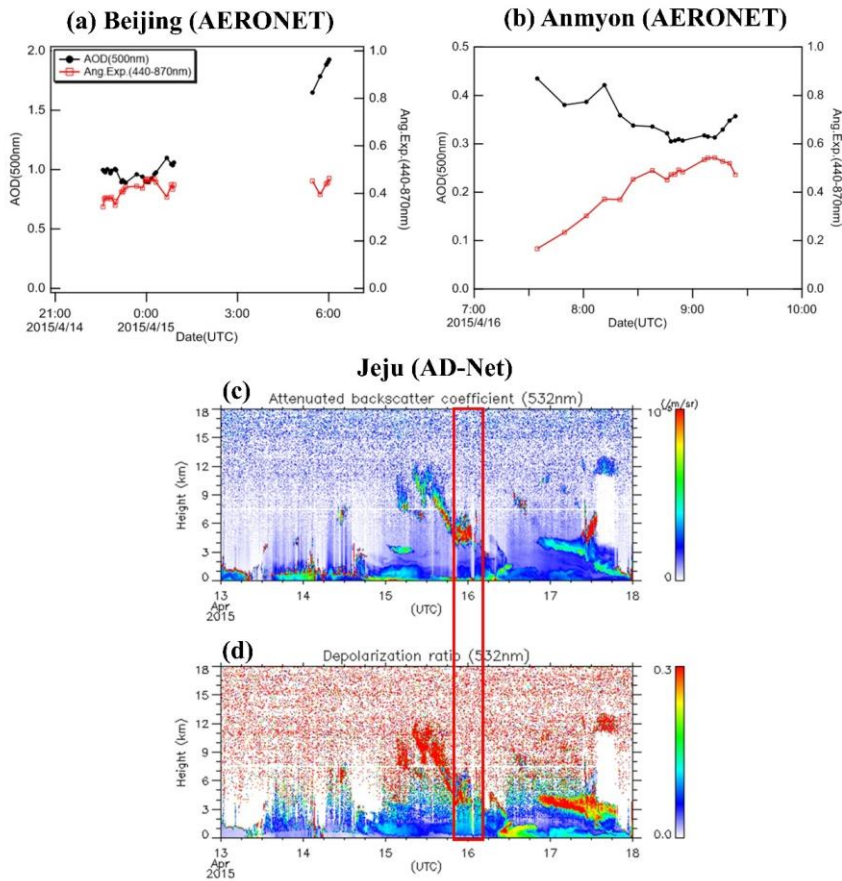
367 vice versa. In general, $AE < 1$ suggested the dominance of coarse particles, which were
368 usually associated with dust or sea salts. While $AE > 1$ suggested the dominance of fine
369 particles, which derived from anthropogenic emissions and biomass burning.

370 As shown in Figure 6a, AOD over Beijing doubled from about 1.0 at around 0:00
371 on April 15 to nearly 2.0 at around 6:00, while $AE_{(440-870nm)}$ remained below 0.5.
372 When the air masses passed over Anmyon, Korea, AOD was about 0.4 at 8:00 on April
373 16 (Figure 6b). AOD at Anmyon was much lower compared to Beijing, which should
374 be due to the removal process during the transport and lower local emissions at Anmyon.
375 Similarly, AE at this site was low below 0.4 and it slightly increased to above 0.5 after
376 8:00. As a whole, the observation of high AOD and low AE at both sites indicated that
377 the air masses contained abundant coarse dust aerosols.

378 Figure 6c shows the vertical profiles of aerosol optical properties over Jeju Island,
379 Korea. The depolarization ratio represents the degree of particle approximation to a
380 sphere in the range of 0 - 1. The depolarization ratio of a spherical object is equal to 0,
381 and vice versa (Mishra et al., 2010). Since dust aerosols were irregularly shaped
382 particles, the depolarization ratio of dust aerosols usually ranged between 0.2 and 0.3.
383 As for the intense dust storm events, the depolarization ratio of particles could reach
384 over 0.4 (Liu et al., 2003). High extinction coefficients and depolarization ratios
385 between 0.1 and 0.3 at around 4 km over Jeju in the early morning of April 16, 2015
386 were observed. By comparing the simulated height of the air mass backward trajectory
387 and the observed plume height over Jeju, good agreement was found (Figure 4b),
388 corroborating the same origin of the Arctic pollution and the Asian downstream dust

389 plumes.

390



391

392 **Figure 6. Aerosol optical properties observed at ground-based sites during CASE**

393 **I. (a) AOD (500nm) and Angström exponent (440-870nm) at the Beijing**

394 **AERONET site. (b) AOD and Angström exponent at the Anmyon AERONET site.**

395 **Vertical profiles of (c) backscattering coefficient and (d) depolarization ratio at the**

396 **Jeju AD-Net site. The red rectangle denotes the time when dust passed over the**

397 **site. Clouds are screened and represented by the blank pixels.**

398

399 After April 16, the dust plume moved towards Russia and the North Pacific. Due

400 to the lacking of ground-based observations in this region, CALIPSO inversion

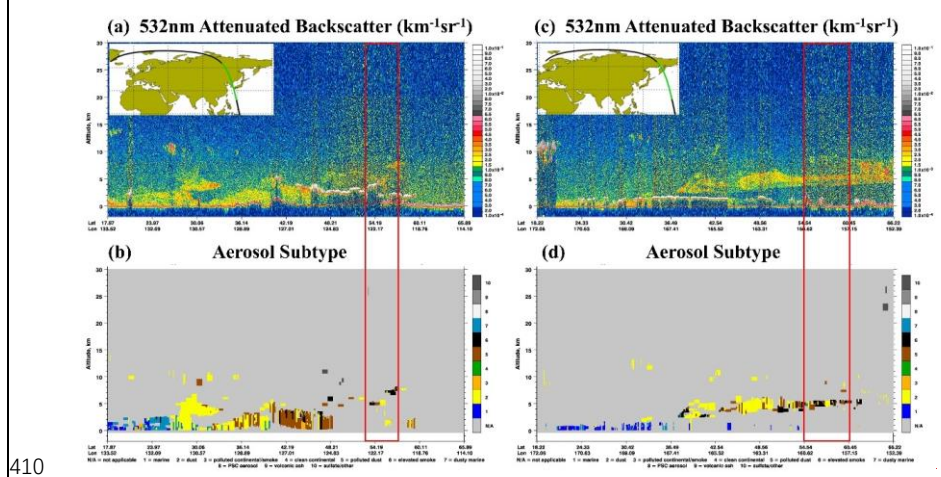
Formatted: Font: Bold

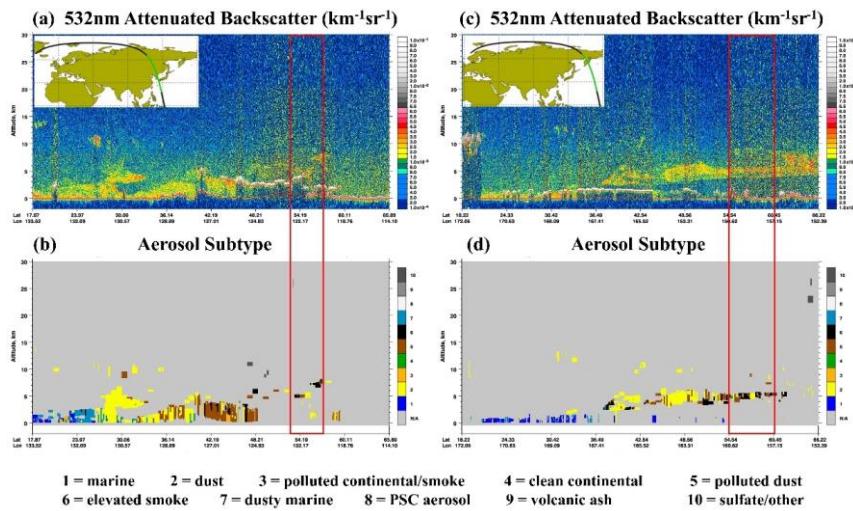
Formatted: Font: Bold, Font color: Auto

Formatted: Font: Bold

Formatted: Font: Bold, Font color: Auto

401 products were used to fill in these blank regions. At about 5:00 UTC on April 17, 2015,
 402 over the northeastern part of Russia (54.19°N, 122.17°E), CALIPSO observed an
 403 aerosol layer, about 5 km above the ground. This height was generally consistent with
 404 that of the simulated backward trajectory (Figure 4b) and the plume was identified as a
 405 mixture of dust, polluted dust, and other types of aerosols (Figure 7). At 2:00 UTC on
 406 April 18, CALIPSO observed a similar mixed layer of dust, polluting dust, and lifted
 407 smoke at 4-6 km over the Kamchatka Peninsula in Russia (Figure 7). Compared to the
 408 previous day, the lifted smoke was more abundant, suggesting that smoke aerosols from
 409 forest fires may have been mixed with the air masses passed over Russia.





411

412

413

414

415

416

417 **(ii) CASE II**

418

419

420

421

422

423

424

425

426

427

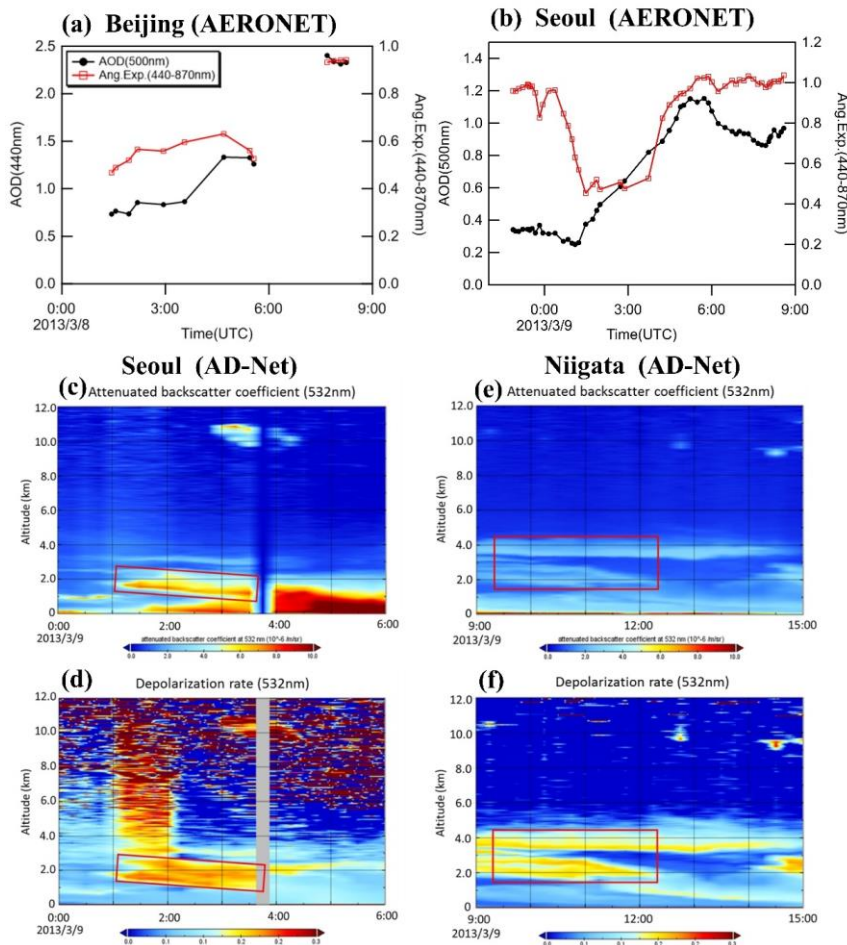
Figure 7. CALIPSO profiles of aerosol backscattering coefficients and identified aerosol types on April 17 (a-b) and 18 (c-d), 2015. The red rectangles denote the regions as indicated by the CALIPSO tracks in Figure 4a.

Figure 8 shows the available ground-based observations close to the transport pathway during CASE II. At the Beijing AERONET site, at 3:00 UTC on March 8, 2013, AOD was 0.73 while AE was 0.47. This was indicative of the dominance of dust particles. Afterwards at 8:00, AOD increased more than twice and approached 2.5, while AE also increased to more than 0.9, indicating that the dust in CASE II was more mixed with fine particles than CASE I.

From 0:00 to 6:00 UTC on March 9, 2013, observed AE at the Seoul AERONET site decreased to a low level of about 0.6 and increased to around 1.0 for several hours. This process was accompanied by a continuous increase of AOD, reaching a maximum of 1.15. In addition, the vertical profiles of the aerosol optical properties in the early

428 morning of March 9 indicated a 1-2 km thick dust layer at altitudes of 1-3 km height
429 over Seoul (Figure 8c), which was in good agreement with the height of the backward
430 trajectory (Figure 5b). Figure 8d shows the lidar vertical observations in Niigata, Japan.
431 A 1-2km thick dust layer at altitudes of 2 – 4km was also observed at 9:00-12:00 UTC
432 on March 9. The heights of the dust layers observed from lidars were also in good
433 agreement with the time and height of the simulated backward trajectory as shown in
434 Figure 5b.

435



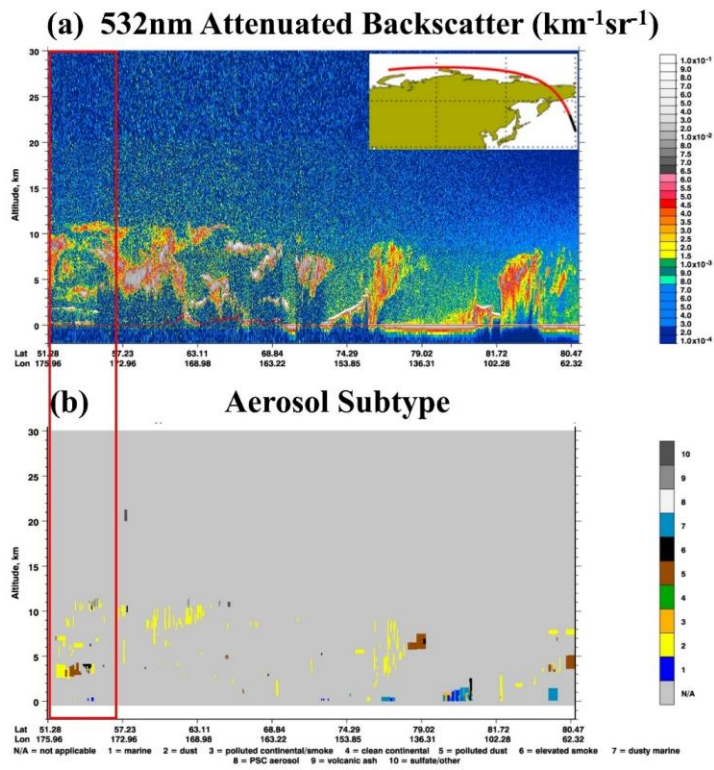
436
 437 **Figure 8. Aerosol optical properties observed at ground-based sites during CASE**
 438 **II. (a) AOD (550nm) and Angström exponent (440-870nm) at the Beijing**
 439 **AERONET site (b) AOD and Angström exponent at the Seoul AERONET site (c-**
 440 **d) Vertical profiles of backscattering coefficient and depolarization ratio at the**
 441 **Seoul AD-Net site (e-f) Vertical profiles of backscattering coefficient and**
 442 **depolarization ratio at the Niigata AD-Net site. The red rectangle denotes the time**
 443 **when dust passed over the site.**

Formatted: Font: Bold

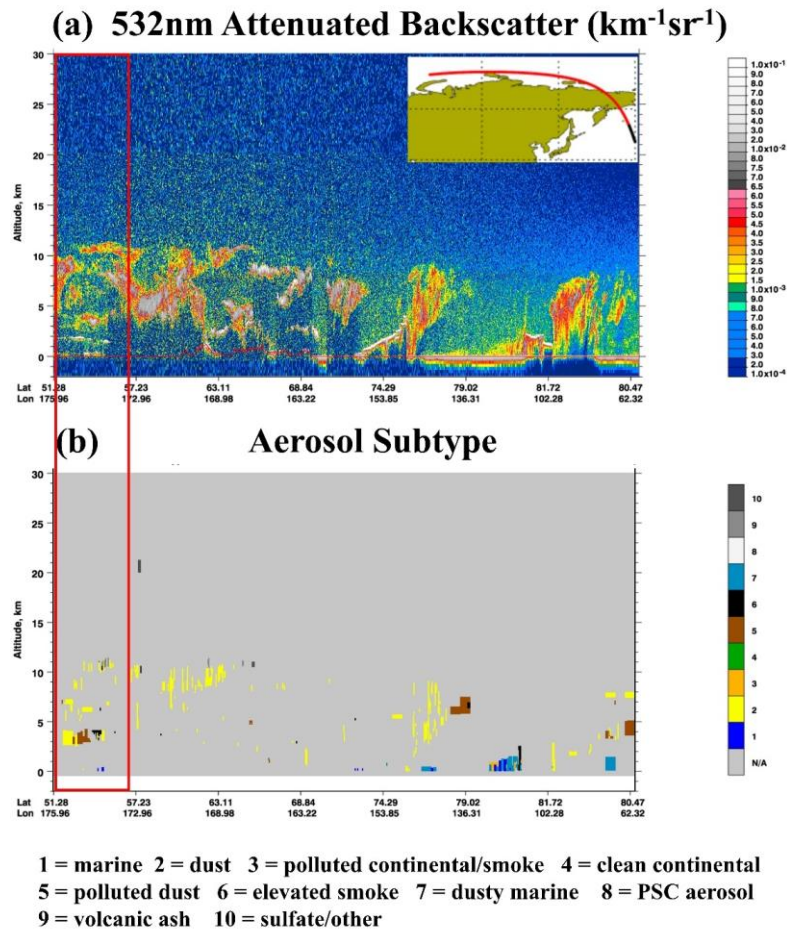
444

445 Figure 9 shows the aerosol vertical structure observed from CALIPSO over the
 446 Bering Sea (51.28°N, 175.96°E - 57.23°N, 172.96°E) on March 12, 2013. At around
 447 2.5 - 4 km, an aerosol layer was evident, consisting of dust and polluted dust,

448 confirming that the aerosols transported to the remote ocean still contained a large
 449 amount of dust particles.



450



451

452

453 **Figure 9. CALIPSO profiles of (a) aerosol backscattering coefficients and (b)**
 454 **identified aerosol types on March 12, 2013. The red rectangles denote the regions**
 455 **as indicated by the CALIPSO tracks in Figure 5a.**

456

457 By comparing the transport pathways of CASE I and CASE II, CASE I passed
 458 over more terrestrial areas, increasing the probability of mixing between dust and air
 459 pollutants from anthropogenic emissions. While CASE II travelled more over the open
 460 ocean, which was more likely to mix with sea salts. In terms of transport time, the air

461 masses in CASE I took about four days to reach the receptor after getting out of the
462 Asian dust source regions, while the air masses in CASE II took about six days. The
463 longer transport time in CASE II may lead to more deposition of coarse dust particles
464 due to the gravitational effect and other removing processes such as wet scavenging.

465

466 **3.6 Evolution of aerosol optical properties during long-range transport to the** 467 **Arctic**

468 In the previous section, it has been well demonstrated that the Arctic air pollution events
469 in both CASE I and CASE II were caused by the long-range transport of Asian dust.
470 However, only a limited observation from ground-based sites and CALIPSO was
471 available for the analysis of aerosol properties. In order to analyze the evolution of
472 aerosols during the transport, MODIS data with a wide spatial coverage was used to
473 quantify the changes of aerosol optical properties.

474 As shown in Figure S1, MODIS data were analyzed on a daily basis. Since
475 simulated backward trajectories were subject to certain uncertainties (Draxler and Hess,
476 1998), the rectangular subsection that covered the daily trajectory was extracted to
477 represent the aerosol properties along the transport pathway. Figure 10 compares the
478 mean values of AOD and AE over the daily transport coverage area between the two
479 cases. As shown in Figure 10a, AOD in CASE I exhibited an evidently decreasing trend
480 with time. It averaged 0.86 on April 14, 2015 over the dust source regions, while it was
481 0.10 at Barrow on April 20, indicating a tremendous AOD decrease of nearly 8 times.
482 In the meanwhile, AE showed an increasing trend (Figure 10b). This indicated that, on

483 the one hand, the high aerosol concentrations from the dust source regions had been
484 significantly eliminated by various physical scavenging processes. In the meantime,
485 local air pollutants could be reduced by the strongly invaded dust (Wang et al., 2018a).
486 On the other hand, dust mixed with fine particles such as black carbon, nitrate, and
487 sulfate and gradually modified the irregular dust particles to be more spheric (Xu et al.,
488 2020).

489 In contrast, less variation of AOD during the transport was observed in CASE II
490 (Figure 10c). AOD was relatively low over the Gobi Desert on March 7 while t~~The~~
491 ~~level of mean AOD even increased to~~stayed in the range of 0.56 - 0.68 from March 8
492 to 11. As shown in Figure S1b, the eastward movement of aerosol plume was evident.
493 This probably indicated the dust plume had already drifted away from the dust source
494 region, which explained the lower AOD in the source region than the downwind regions.
495 Meanwhile, except for the low value of AE on March 8 (possibly due to the small
496 number of data points as shown in Figure S1b), the mean AE values were above 1.0 on
497 March 7 and 9. This suggested that dust mixed with more fine particles and coarse
498 particles were more removed. Overall, by comparing these two cases, it was evident
499 that different transport routes to the Arctic had divergent effects on the evolution of
500 aerosol optical properties.

501

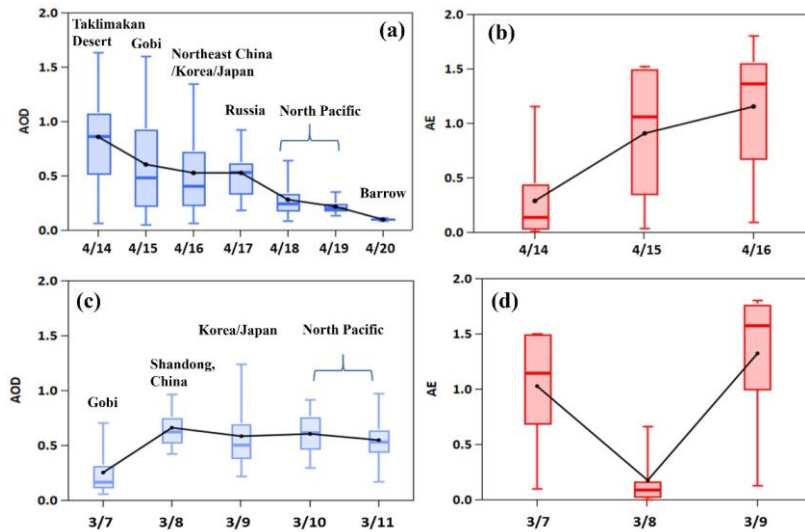


Figure 10. Regional (a) AOD and (b) Angström exponent in CASE I. Regional (c) AOD and (d) Angström exponent in CASE II. The dots and lines inside the boxes represent the mean and median values, respectively; bottom and top of the boxes represent the 25 and 75% limits, respectively; and bottom and top short lines represent the minimum and maximum values, respectively. The geographic region in each day is defined in Figure S1.

3.7 Impact assessment of transported aerosols on the Arctic surface albedo

Surface albedo is an important parameter for energy exchange between the surface and the atmosphere in polar regions. The changes in snow and ice albedos could have important climatic impacts on the polar regions as well as the whole world. Due to the large difference between the multiple scattering effect of snow and ice and absorption effects of absorbing impurities (e.g. black carbon and dust), very small amounts of deposited impurities can lead to a decrease of snow and ice albedo (Zhang et al., 2017). Hansen and Nazarenko (2004) showed that the effect of soot on reducing snow and ice albedo was around 1.5% in the Arctic and 3% in the snow and ice covered areas of the

520 Northern Hemisphere. Kaspari et al. (2014) showed that black carbon reduced snow
521 and ice albedo by 6-10% relative to pure snow in the Himalayas in winter and spring,
522 and other impurities such as dust even reduced snow and ice albedo by 40 - 42%. In
523 this regard, decreases of snow and ice albedo would cause surface warming, thinning
524 of sea ice, melting permafrost, and consequently sea level rise that may have serious
525 impacts on the global water resources and ecosystems.

526 In this section, the impacts of the two Arctic pollution events on changing the surface
527 albedo were assessed. The SNICAR snow and ice albedo model was applied to estimate
528 the contributions of dust and black carbon to the reduction of snow and ice albedo.

529

530 **3.7.1 Estimation of mass concentrations of impurities in snow and evaluation of** 531 **model performance**

532 In this study, we only considered airborne dust and elemental carbon (EC) as the
533 dominant contributors to the impurities in the Arctic snow and ice. Firstly, the
534 atmospheric concentrations of absorbing aerosols were estimated by using the revised
535 IMPROVE (The Interagency Monitoring of Protected Visual Environments) Equation
536 (Pitchford et al., 2007). It was assumed that airborne dust and EC dominated the
537 scattering of coarse particles and absorption of fine particles, respectively (Eq. 1-2).

$$538 C_{\text{dust}} = b_{\text{sca},(\text{PM}_{10} - \text{PM}_1)} / 0.6, \quad (1)$$

$$539 C_{\text{EC}} = b_{\text{abs},\text{PM}_1} / 10, \quad (2)$$

540 Of which, the constant 0.6 and 10 (m^2/g) is the mass scattering efficiency and mass
541 absorption efficiency of dust and EC, respectively (Pitchford et al., 2007). Since the

542 concentrations of impurities in snow were required as inputs for the SNICAR model,
543 we estimated them based on the following assumption. Dou et al. (2017) conducted
544 field sampling at Barrow during April and May in 2015 and measured elemental carbon
545 concentration of 3.30 ng/g in the snow sample on April 30, 2015. The airborne
546 elemental carbon concentration was estimated to be 6.25 ng/m³ on the same day by
547 using the equations above. Thus, the ratio of the particulate matter in the snow versus
548 that in the atmosphere was calculated to be 0.528m³/g. This ratio was then applied to
549 estimate the concentrations of dust and elemental carbon in snow during the two cases
550 based on the assumption that particulate dust and elemental carbon could be well mixed
551 under the sufficiently long transport duration.- Since the cumulative effect of impurities
552 in reducing the surface albedo was not considered in this study, the simulation result by
553 the SNICAR model was considered as the instantaneous surface albedo in the following
554 discussions.

555 To evaluate the model performance, Figure S2 compares the simulated values of
556 surface albedo and the observations at an ARM (Atmospheric Radiation Measurement)
557 site located at Barrow during 14 – 19, April, 2015. A correlation coefficient of 0.74 was
558 derived, indicating the relatively good model performance on simulating the Arctic
559 surface albedo. However, deviations of simulated values from observations were still
560 found. The bias may derive from the following aspects. First, the concentrations of dust
561 and elemental carbon in snow as inputs for the model were not in-situ measured, as well
562 as for the other input parameters such as snow radius, thickness, and density. Secondly,
563 the simulation only considered the absorbing substances deposited from the atmosphere

564 while the pre-existing impurities in snow and ice were ignored. Last but not the least,
565 impurities such as brown carbon were not included for the simulation.

566

567 **3.7.2 Comparison of the changes of Arctic surface albedo between two cases**

568 In this section, the impacts of transported particles on the change of surface albedo in
569 both cases were evaluated. Figure S3 shows the time-series of estimated dust and
570 elemental carbon in snow during the two pollution cases. As for CASE I (Figure S3a),
571 the peak time of elemental carbon was about half a day ahead of that of dust. This
572 phenomenon was as similar as some other dust events that anthropogenic air pollutants
573 were ahead of dust pushed by the cold front (Guo et al., 2004; Wang et al., 2018a). In
574 regard of the variations of pollutants, four representative moments were selected, i.e.,
575 0:00 on April 18 (the beginning of pollution), 13:00 on April 19 (the peak time of
576 elemental carbon), 3:00 on April 20 (the peak time of dust), and 15:00 on April 21 (the
577 end of pollution). As for CASE II (Figure S3b), the estimated concentrations of
578 impurities in snow stayed at relatively low levels and varied less strongly compared to
579 CASE I. We chose 12:00 on March 14 (the beginning of pollution), 17:00 on March 15
580 (the peak time of dust), and 13:00 on March 18 (the end of pollution) for the analysis.

581 By using the SNICAR model, the effects of dust, elemental carbon, and
582 combination of dust and elemental carbon on the surface albedo were separately
583 assessed. As shown in Table 4, the reduction of surface albedo caused by long-range
584 transported Asian light-absorbing pollutants ranged from 0.35% to 2.63%, which were
585 consistent with previous studies. For instance, Dou et al. (2017) calculated a 1.6-5.1%

586 reduction in snow and ice albedo caused by dust and black carbon at Barrow from late
587 April to May 2015, with a 5-10 fold increase in pollutant concentrations compared to
588 the pre-April period due to the snowmelt period during that time. Zhang et al. (2017)
589 calculated that dust and black carbon reduced snow and ice albedo by 0.72-1.00% on
590 glaciers in the southeastern Tibetan Plateau in June 2015. In CASE I, the highest
591 concentration of elemental carbon in snow reached more than 72 ng/g, which could
592 reduce the albedo by 1.47%. And the highest concentration of dust reached more than
593 37 $\mu\text{g/g}$, which could reduce the albedo by 2.26%. During this pollution event, the
594 combined effect of dust and elemental carbon significantly reduced the snow and ice
595 albedo by 2.28%. In CASE II, elemental carbon concentrations were much lower than
596 CASE I and its effect on albedo was below 0.40%, while dust can reduce albedo up to
597 1.87%. The combined effect of dust and elemental carbon reached more than 2%
598 compared to the pure snow condition.

599

600 **Table 4. Simulated changes of albedo due to dust, elemental carbon, and**
601 **combination of dust and elemental carbon (SA represents the simulated surface**
602 **albedo of pure snow)**

Time (UTC)	BC snow (ng/g)	Dust snow (µg/g)	SA Pure	SA+EC	SA+Dust	SA+EC & Dust	EC (%)	Dust (%)	EC&Dust (%)
Barrow									
2015/4/18 0:00	24.31	8.31	0.7990	0.7901	0.7915	0.7852	1.12%	0.94%	1.73%
2015/4/15 15:00	72.14	21.39	0.8392	0.8270	0.8300	0.8218	1.47%	1.10%	2.07%
2015/4/20 3:00	21.16	37.11	0.8143	0.8077	0.7959	0.7929	0.83%	2.26%	2.63%
2015/4/21 15:00	6.08	1.93	0.8379	0.8361	0.8365	0.8350	0.22%	0.17%	0.35%
Alert									
2013/3/14 13:00	7.75	10.77	0.7995	0.7964	0.7912	0.7891	0.39%	1.04%	1.30%
2013/3/15 17:00	7.37	20.74	0.7923	0.7892	0.7775	0.7758	0.40%	1.87%	2.08%
2013/3/18 13:00	6.52	3.68	0.7956	0.7929	0.7921	0.7899	0.34%	0.44%	0.72%

604 As discussed above, the concentrations of dust and elemental carbon were
605 relatively higher in CASE I, hence the resulting effects on snow and ice albedo were
606 more obvious. On the one hand, the transport time in CASE I was shorter and the
607 particulate matters were scavenged less along the transport. On the other hand, the air
608 masses in CASE I passed over a large number of terrestrial areas, including northeast
609 China and Siberia. Fine particles from anthropogenic emissions and biomass burning
610 in Siberia mixed with dust and transported to Barrow together, making the elemental
611 carbon at the receptor significantly higher. As for CASE II, the receptor site at Alert is
612 a higher latitudinal area, which was much less affected by local anthropogenic activities.
613 In addition, the transport pathway of CASE II was mostly over the open ocean with

614 longer duration. This finally induced much lower air pollutant concentrations and
615 weaker impact on the reduction of surface albedo.

616

617 **4. Conclusions**

618 In this study, the long-range transport of Asian dust to the Arctic was investigated.

619 During 2011-2015, 50 dust events in China were recorded, of which 38 dust events had

620 the capability to reach the Arctic based on the air mass trajectory simulation. Two main

621 transport routes were identified. One typical transport type was characterized of wide

622 geographic coverage, long transport duration (generally 7-10 days), and mainly marine

623 transport due to the high lifting altitude of dust particles (mostly over 1500m) over the

624 dust source regions. The other typical transport type was characterized of dust transport

625 mostly over land with relatively short duration of about 4-8 days. This was due to the

626 presence of a low-pressure system over northern Japan in spring, which induced the air

627 masses deflecting northward.

628 Two typical coarse particle dominated cases observed in the Arctic were

629 specifically investigated, i.e., one at Barrow in April 2015 (CASE I) and the other one

630 at Alert in March 2013 (CASE II), respectively. Based on the air mass trajectory

631 simulation, in CASE I, dust originated from the Taklamakan and Gobi deserts in China,

632 then passed over East Asia, Siberia of Russia, and the Pacific Ocean, and finally reached

633 Barrow. In CASE II, dust originated from the Gobi Desert, then passed over Korea and

634 Japan and directly entered the Pacific Ocean, and finally moved northward across the

635 Arctic Ocean and reached Alert.

636 The dust transport pathways during both cases were verified based on a synergy
637 of NCEP reanalysis data (geopotential height fields), ground-based observations
638 (AERONET aerosol columnar properties and lidar aerosol profiles), and satellite
639 products (CALIPSO profiles). The passing time and height of the dust plume based on
640 trajectory simulation coincided very consistently with various observations. The
641 evolution of aerosol optical properties during the transport was assessed by using the
642 large-scale MODIS data. In CASE I, AOD showed a significant decreasing trend while
643 Angström exponent showed an increasing trend from the dust source region to the
644 receptor. In contrast, AOD varied much less significantly in CASE II. It was evident
645 that different transport routes to the Arctic had divergent effects on the evolution of
646 aerosol properties.

647 The SNICAR snow and ice model was applied to simulate the impact of impurities
648 on the reduction of surface albedo in the Arctic during the two cases. The concentrations
649 of dust and elemental carbon in snow were estimated and the effects of dust, elemental
650 carbon, and combination of dust and elemental carbon on snow and ice albedo were
651 separately quantified. The reduction of snow and ice albedo caused by long-range
652 transported Asian light-absorbing pollutants ranged from 0.35% to 2.63%. This study
653 highlighted that the long-range transport of Asian dust to the Arctic was ubiquitous and
654 its impact on changing the radiative forcing and regional climate in the Arctic should
655 be considered by the atmosphere-ocean-cryosphere interaction.

656 It has to be noted that the simulation of surface albedo due to the transport of dust
657 particles was subject to large uncertainties. The concentrations of impurities in snow

Formatted: Font color: Auto

Formatted: Indent: First line: 2 ch, Line spacing: Double

658 were estimated by empirical equations but not in-situ measurement data. As a result,
659 the cumulative effect of impurities in reducing the surface albedo was not considered.
660 Also, the evolution of dust microphysical properties was not accounted in the model
661 simulation. The atmospheric aging processes, i.e., dust particles coated with various
662 type of aerosols during the long-range transport, could further enhance the reduction of
663 snow albedo. The dust particle refractive index is regarded as an important factor for
664 dust absorption in snowpack (He, 2022). To reduce the uncertainties of snow albedo
665 simulation, simultaneous in-situ measurements of particle composition and optical
666 properties in both the air and snowpack are essentially needed in the future Arctic
667 studies.

Formatted: Default Paragraph Font, Font color: Auto, Pattern: Clear

Formatted: Font color: Auto

668

669 **Data availability**

670 The measurement data at Barrow and Alert are from the EBAS database
671 (<https://ebas.nilu.no/>). Aerosol columnar data are from AERONET
672 (<https://aeronet.gsfc.nasa.gov/>). Aerosol vertical profiles are from AD-Net
673 (<https://www-lidar.nies.go.jp/AD-Net>). The MODIS Level-3 aerosol products are
674 from NASA's Giovanni (<https://giovanni.gsfc.nasa.gov/giovanni/>). The NCEP/NCAR
675 reanalysis data are from <https://www.esrl.noaa.gov/psd/data/gridded/reanalysis/>

676

677 **Author contributions**

678 KH designed this study. XZ analyzed data. All reviewed and wrote the paper.

679

680 **Competing interests**

681 The authors declare that they have no conflict of interest.

682

683 **Acknowledgements**

684 We sincerely thank for EBAS, AERONET, AD-Net, NASA, and NCEP/NCAR for
685 providing the observational and modeling data. This work was supported by the
686 National Natural Science Foundation of China (42175119, 91644105) and the National
687 Natural Science Foundation of Shanghai (18230722600). Kan Huang also
688 acknowledges Jiangsu Shuangchuang Program through Jiangsu Fuyu Environmental
689 Technology Co., Ltd.

690

691 **References:**

692 Blanchet, J. P. and List, R.: Estimation of optical properties of arctic haze using a numerical model,
693 *Atmosphere-Ocean*, 21, 444-465, 10.1080/07055900.1983.9649179, 2010.

694 Breider, T. J., Mickley, L. J., Jacob, D. J., Ge, C., Wang, J., Sulprizio, M. P., Croft, B., Ridley, D. A.,
695 McConnell, J. R., Sharma, S., Husain, L., Dutkiewicz, V. A., Eleftheriadis, K., Skov, H., and Hopke, P.
696 K.: Multidecadal trends in aerosol radiative forcing over the Arctic: Contribution of changes in
697 anthropogenic aerosol to Arctic warming since 1980, *Journal of Geophysical Research-*
698 *Atmospheres*, 122, 3573-3594, 10.1002/2016jd025321, 2017.

699 Brock, C. A., Cozic, J., Bahreini, R., Froyd, K. D., Middlebrook, A. M., McComiskey, A., Brioude, J.,
700 Cooper, O. R., Stohl, A., Aikin, K. C., de Gouw, J. A., Fahey, D. W., Ferrare, R. A., Gao, R. S., Gore, W.,
701 Holloway, J. S., Huebler, G., Jefferson, A., Lack, D. A., Lance, S., Moore, R. H., Murphy, D. M., Nenes,
702 A., Novelli, P. C., Nowak, J. B., Ogren, J. A., Peischl, J., Pierce, R. B., Pilewskie, P., Quinn, P. K., Ryerson,
703 T. B., Schmidt, K. S., Schwarz, J. P., Sodemann, H., Spackman, J. R., Stark, H., Thomson, D. S.,
704 Thornberry, T., Veres, P., Watts, L. A., Warneke, C., and Wollny, A. G.: Characteristics, sources, and
705 transport of aerosols measured in spring 2008 during the aerosol, radiation, and cloud processes
706 affecting Arctic Climate (ARCPAC) Project, *Atmospheric Chemistry and Physics*, 11, 2423-2453,
707 10.5194/acp-11-2423-2011, 2011.

708 CMA: (China Meteorological Administration Eds.): *Sand-dust Weather Almanac (2011)*, China
709 Meteorological Press, Beijing, China, 2013.

710 CMA: (China Meteorological Administration Eds.): *Sand-dust Weather Almanac (2012)*, China
711 Meteorological Press, Beijing, China, 2014.

712 CMA: (China Meteorological Administration Eds.): Sand-dust Weather Almanac (2013), China
713 Meteorological Press, Beijing, China, 2015.
714 CMA: (China Meteorological Administration Eds.): Sand-dust Weather Almanac (2014), China
715 Meteorological Press, Beijing, China, 2016.
716 CMA: (China Meteorological Administration Eds.): Sand-dust Weather Almanac (2015), China
717 Meteorological Press, Beijing, China, 2017.
718 Dagsson-Waldhauserova, P., Renard, J. B., Olafsson, H., Vignelles, D., Berthet, G., Verdier, N., and
719 Duverger, V.: Vertical distribution of aerosols in dust storms during the Arctic winter, *Sci Rep-Uk*,
720 9, 2019.
721 Di Biagio, C., Pelon, J., Ancellet, G., Bazureau, A., and Mariage, V.: Sources, Load, Vertical
722 Distribution, and Fate of Wintertime Aerosols North of Svalbard From Combined V4 CALIOP Data,
723 Ground-Based IAOS Lidar Observations and Trajectory Analysis, *Journal of Geophysical*
724 *Research-Atmospheres*, 123, 1363-1383, 10.1002/2017jd027530, 2018.
725 Di Pierro, M., Jaegle, L., and Anderson, T. L.: Satellite observations of aerosol transport from East
726 Asia to the Arctic: three case studies, *Atmospheric Chemistry and Physics*, 11, 2225-2243,
727 10.5194/acp-11-2225-2011, 2011.
728 Domine, F., Cabanes, A., and Legagneux, L.: Structure, microphysics, and surface area of the Arctic
729 snowpack near Alert during the ALERT 2000 campaign, *Atmospheric Environment*, 36, 2753-2765,
730 10.1016/s1352-2310(02)00108-5, 2002.
731 Dong, X., Xi, B., Crosby, K., Long, C. N., Stone, R. S., and Shupe, M. D.: A 10 year climatology of
732 Arctic cloud fraction and radiative forcing at Barrow, Alaska, *Journal of Geophysical Research-*
733 *Atmospheres*, 115, 10.1029/2009jd013489, 2010.
734 Dou, T., Xiao, C., Du, Z., Schauer, J. J., Ren, H., Ge, B., Xie, A., Tan, J., Fu, P., and Zhang, Y.: Sources,
735 evolution and impacts of EC and OC in snow on sea ice: a measurement study in Barrow, Alaska,
736 *Science Bulletin*, 62, 1547-1554, 10.1016/j.scib.2017.10.014, 2017.
737 Draxier, R. R. and Hess, G. D.: An overview of the HYSPLIT₄ modelling system for trajectories,
738 dispersion and deposition, *Aust Meteorol Mag*, 47, 295-308, 1998.
739 Fan, S. M.: Modeling of observed mineral dust aerosols in the arctic and the impact on winter
740 season low-level clouds, *J Geophys Res-Atmos*, 118, 11161-11174, 2013.
741 Ferrero, L., Ritter, C., Cappelletti, D., Moroni, B., Mocnik, G., Mazzola, M., Lupi, A., Becagli, S.,
742 Traversi, R., Cataldi, M., Neuber, R., Vitale, V., and Bolzacchini, E.: Aerosol optical properties in the
743 Arctic: The role of aerosol chemistry and dust composition in a closure experiment between Lidar
744 and tethered balloon vertical profiles, *Sci Total Environ*, 686, 452-467, 2019.
745 Fisher, J. A., Jacob, D. J., Wang, Q., Bahreini, R., Carouge, C. C., Cubison, M. J., Dibb, J. E., Diehl, T.,
746 Jimenez, J. L., Leibensperger, E. M., Lu, Z., Meinders, M. B. J., Pye, H. O. T., Quinn, P. K., Sharma, S.,
747 Streets, D. G., van Donkelaar, A., and Yantosca, R. M.: Sources, distribution, and acidity of sulfate-
748 ammonium aerosol in the Arctic in winter-spring, *Atmospheric Environment*, 45, 7301-7318,
749 10.1016/j.atmosenv.2011.08.030, 2011.
750 Flanner, M. G.: Arctic climate sensitivity to local black carbon, *Journal of Geophysical Research-*
751 *Atmospheres*, 118, 1840-1851, 10.1002/jgrd.50176, 2013.
752 Flanner, M. G., Zender, C. S., Randerson, J. T., and Rasch, P. J.: Present-day climate forcing and
753 response from black carbon in snow, *Journal of Geophysical Research-Atmospheres*, 112,
754 10.1029/2006jd008003, 2007.
755 Gagne, M.-E., Fyfe, J. C., Gillett, N. P., Polyakov, I. V., and Flato, G. M.: Aerosol-driven increase in

756 Arctic sea ice over the middle of the twentieth century, *Geophysical Research Letters*, 44, 7338-
757 7346, 10.1002/2016gl071941, 2017.

758 Gillett, N. P., Stone, D. A., Stott, P. A., Nozawa, T., Karpechko, A. Y., Hegerl, G. C., Wehner, M. F.,
759 and Jones, P. D.: Attribution of polar warming to human influence, *Nature Geoscience*, 1, 750-754,
760 10.1038/ngeo338, 2008.

761 Ginoux, P., Prospero, J. M., Gill, T. E., Hsu, N. C., and Zhao, M.: Global-Scale Attribution of
762 Anthropogenic and Natural Dust Sources and Their Emission Rates Based on Modis Deep Blue
763 Aerosol Products, *Rev Geophys*, 50, 2012.

764 Guo, J., Rahn, K. A., and Zhuang, G. S.: A mechanism for the increase of pollution elements in dust
765 storms in Beijing, *Atmos. Environ.*, 38, 855-862, 2004.

766 Guo, J., Lou, M., Miao, Y., Wang, Y., Zeng, Z., Liu, H., He, J., Xu, H., Wang, F., Min, M., and Zhai, P.:
767 Trans-Pacific transport of dust aerosols from East Asia: Insights gained from multiple observations
768 and modeling, *Environmental Pollution*, 230, 1030-1039, 10.1016/j.envpol.2017.07.062, 2017.

769 Hansen, J. and Nazarenko, L.: Soot climate forcing via snow and ice albedos, *Proceedings of the*
770 *National Academy of Sciences of the United States of America*, 101, 423-428,
771 10.1073/pnas.2237157100, 2004.

772 He, C.: Modelling light-absorbing particle-snow-radiation interactions and impacts on
773 snow albedo: fundamentals, recent advances and future directions, *Environmental*
774 *Chemistry*, 10.1071/EN22013, 2022.

775 Holben, B. N., Eck, T. F., Slutsker, I., Tanre, D., Buis, J. P., Setzer, A., Vermote, E., Reagan, J. A.,
776 Kaufman, Y. J., Nakajima, T., Lavenu, F., Jankowiak, I., and Smirnov, A.: AERONET - A federated
777 instrument network and data archive for aerosol characterization, *Remote Sens Environ*, 66, 1-16,
778 Doi 10.1016/S0034-4257(98)00031-5, 1998.

779 Hsu, N. C., M.-J. Jeong, C. Bettenhausen, A. M. Sayer, R. Hansell, C. S. Seftor, J.
780 Huang, and S.-C. Tsay (2013), Enhanced Deep Blue aerosol retrieval algorithm: The
781 second generation, *J. Geophys. Res. Atmos.*, 118, 9296-9315, doi:10.1002/jgrd.50712.

782 Huang, Z., Huang, J., Hayasaka, T., Wang, S., Zhou, T., and Jin, H.: Short-cut transport path for
783 Asian dust directly to the Arctic: a case study, *Environmental Research Letters*, 10, 10.1088/1748-
784 9326/10/11/114018, 2015a.

785 Huang, Z. W., Huang, J. P., Hayasaka, T., Wang, S. S., Zhou, T., and Jin, H. C.: Short-cut transport
786 path for Asian dust directly to the Arctic: a case study, *Environ Res Lett*, 10, 2015b.

787 Kaspari, S., Painter, T. H., Gysel, M., Skiles, S. M., and Schwikowski, M.: Seasonal and elevational
788 variations of black carbon and dust in snow and ice in the Solu-Khumbu, Nepal and estimated
789 radiative forcings, *Atmospheric Chemistry and Physics*, 14, 8089-8103, 10.5194/acp-14-8089-
790 2014, 2014.

791 Koch, D. and Del Genio, A. D.: Black carbon semi-direct effects on cloud cover: review and synthesis,
792 *Atmospheric Chemistry and Physics*, 10, 7685-7696, 10.5194/acp-10-7685-2010, 2010.

793 Kylling, A., Zwaafink, C. D. G., and Stohl, A.: Mineral Dust Instantaneous Radiative Forcing in the
794 Arctic, *Geophys Res Lett*, 45, 4290-4298, 2018.

795 Levy, R. C., L. A. Remer, S. Mattoo, E. F. Vermote, and Y. J. Kaufman (2007), Second-
796 generation operational algorithm: Retrieval of aerosol properties over land from
797 inversion of Moderate Resolution Imaging Spectroradiometer spectral reflectance, *J.*
798 *Geophys. Res.*, 112, D13211, doi:10.1029/2006JD007811.

799 Liu, D., Qi, F. D., Jin, C. J., Yue, G. M., and Zhou, J.: Polarization lidar observations of cirrus clouds

Formatted: Normal

Formatted: Normal

Formatted: Font: (Default) Times New Roman, 小四, Font color: Blue

800 and Asian dust aerosols over Hefei, Chinese Journal of Atmospheric Sciences, 27, 1093 - 1100,
801 2003.

802 Liu, H., Liu, X. D., and Dong, B. W.: Influence of Central Siberian Snow-Albedo Feedback on the
803 Spring East Asian Dust Cycle and Connection With the Preceding Winter Arctic Oscillation, J
804 Geophys Res-Atmos, 123, 13368-13385, 2018.

805 Marelle, L., Raut, J. C., Thomas, J. L., Law, K. S., Quennehen, B., Ancellet, G., Pelon, J.,
806 Schwarzenboeck, A., and Fast, J. D.: Transport of anthropogenic and biomass burning aerosols
807 from Europe to the Arctic during spring 2008, Atmospheric Chemistry and Physics, 15, 3831-3850,
808 10.5194/acp-15-3831-2015, 2015.

809 Mishra, M. K., Rajeev, K., Thampi, B. V., Parameswaran, K., and Nair, A. K. M.: Micro pulse lidar
810 observations of mineral dust layer in the lower troposphere over the southwest coast of Peninsular
811 India during the Asian summer monsoon season, Journal of Atmospheric and Solar-Terrestrial
812 Physics, 72, 1251-1259, 10.1016/j.jastp.2010.08.012, 2010.

813 [Omar, A. H., et al. \(2009\). The CALIPSO automated aerosol classification and lidar](#)
814 [ratio selection algorithm, J. Atmos. Oceanic Technol.,26,1994-2014,](#)
815 [doi:10.1175/2009JTECHA1231.1.](#)

816 Pitchford, M., Malm, W., Schichtel, B., Kumar, N., Lowenthal, D., and Hand, J.: Revised algorithm for
817 estimating light extinction from IMPROVE particle speciation data, J Air Waste Manage, 57, 1326-
818 1336, 10.3155/1047-3289.57.11.1326, 2007.

819 Qi, L., Li, Q., Henze, D. K., Tseng, H.-L., and He, C.: Sources of springtime surface black carbon in
820 the Arctic: an adjoint analysis for April 2008, Atmospheric Chemistry and Physics, 17, 9697-9716,
821 10.5194/acp-17-9697-2017, 2017.

822 Quinn, P. K., Bates, T. S., Baum, E., Doubleday, N., Fiore, A. M., Flanner, M., Fridlind, A., Garrett, T.
823 J., Koch, D., Menon, S., Shindell, D., Stohl, A., and Warren, S. G.: Short-lived pollutants in the Arctic:
824 their climate impact and possible mitigation strategies, Atmospheric Chemistry and Physics, 8,
825 1723-1735, 10.5194/acp-8-1723-2008, 2008.

826 Ranjbar, K., O'Neill, N. T., Ivanescu, L., King, J., and Hayes, P. L.: Remote sensing of a high-Arctic,
827 local dust event over Lake Hazen (Ellesmere Island, Nunavut, Canada), Atmos Environ, 246, 2021.

828 Sand, M., Berntsen, T. K., Seland, O., and Kristjansson, J. E.: Arctic surface temperature change to
829 emissions of black carbon within Arctic or midlatitudes, Journal of Geophysical Research-
830 Atmospheres, 118, 7788-7798, 10.1002/jgrd.50613, 2013a.

831 Sand, M., Berntsen, T. K., Kay, J. E., Lamarque, J. F., Seland, O., and Kirkevåg, A.: The Arctic response
832 to remote and local forcing of black carbon, Atmospheric Chemistry and Physics, 13, 211-224,
833 10.5194/acp-13-211-2013, 2013b.

834 Screen, J. A. and Simmonds, I.: The central role of diminishing sea ice in recent Arctic temperature
835 amplification, Nature, 464, 1334-1337, 10.1038/nature09051, 2010.

836 Serreze, M. C. and Francis, J. A.: The arctic amplification debate, Climatic Change, 76, 241-264,
837 10.1007/s10584-005-9017-y, 2006.

838 Serreze, M. C., Barrett, A. P., Stroeve, J. C., Kindig, D. N., and Holland, M. M.: The emergence of
839 surface-based Arctic amplification, Cryosphere, 3, 11-19, 10.5194/tc-3-11-2009, 2009.

840 Sharma, S., Ishizawa, M., Chan, D., Lavoue, D., Andrews, E., Eleftheriadis, K., and Maksyutov, S.: 16-
841 year simulation of Arctic black carbon: Transport, source contribution, and sensitivity analysis on
842 deposition, Journal of Geophysical Research-Atmospheres, 118, 943-964, 10.1029/2012jd017774,
843 2013.

Formatted: Normal

844 Shimizu, A., Nishizawa, T., Jin, Y., Kim, S. W., Wang, Z. F., Batdorj, D., and Sugimoto, N.: Evolution
845 of a lidar network for tropospheric aerosol detection in East Asia, *Opt Eng*, 56, 2017.
846 Shindell, D. and Faluvegi, G.: Climate response to regional radiative forcing during the twentieth
847 century, *Nature Geoscience*, 2, 294-300, 10.1038/ngeo473, 2009.
848 Sobhani, N., Kulkarni, S., and Carmichael, G. R.: Source sector and region contributions to black
849 carbon and PM_{2.5} in the Arctic, *Atmospheric Chemistry and Physics*, 18, 18123-18148,
850 10.5194/acp-18-18123-2018, 2018.
851 Stohl, A.: Characteristics of atmospheric transport into the Arctic troposphere, *Journal of*
852 *Geophysical Research-Atmospheres*, 111, 10.1029/2005jd006888, 2006.
853 Stone, R. S., Dutton, E. G., Harris, J. M., and Longenecker, D.: Earlier spring snowmelt in northern
854 Alaska as an indicator of climate change, *Journal of Geophysical Research-Atmospheres*, 107,
855 10.1029/2000jd000286, 2002.
856 Wang, Q., Dong, X., Fu, J. S., Xu, J., Deng, C., Jiang, Y., Fu, Q., Lin, Y., Huang, K., and Zhuang, G.:
857 Environmentally dependent dust chemistry of a super Asian dust storm in March 2010: observation
858 and simulation, *Atmos Chem Phys*, 2018a.
859 Wang, Z., Pan, X., Uno, I., Chen, X., Yamamoto, S., Zheng, H., Li, J., and Wang, Z.: Importance of
860 mineral dust and anthropogenic pollutants mixing during a long-lasting high PM event over East
861 Asia, *Environmental Pollution*, 234, 368-378, 10.1016/j.envpol.2017.11.068, 2018b.
862 Warneke, C., Froyd, K. D., Brioude, J., Bahreini, R., Brock, C. A., Cozic, J., de Gouw, J. A., Fahey, D.
863 W., Ferrare, R., Holloway, J. S., Middlebrook, A. M., Miller, L., Montzka, S., Schwarz, J. P., Sodemann,
864 H., Spackman, J. R., and Stohl, A.: An important contribution to springtime Arctic aerosol from
865 biomass burning in Russia, *Geophysical Research Letters*, 37, 10.1029/2009gl041816, 2010.
866 Weijers, S., Buchwal, A., Blok, D., Loeffler, J., and Elberling, B.: High Arctic summer warming tracked
867 by increased *Cassiope tetragona* growth in the world's northernmost polar desert, *Global Change*
868 *Biology*, 23, 5006-5020, 10.1111/gcb.13747, 2017.
869 Xu, L., Fukushima, S., Sobanska, S., Murata, K., Naganuma, A., Liu, L., Wang, Y., Niu,
870 H., Shi, Z., Kojima, T., Zhang, D., and Li, W.: Tracing the evolution of morphology
871 and mixing state of soot particles along with the movement of an Asian dust
872 storm, *Atmos. Chem. Phys.*, 20, 14321-14332, 10.5194/acp-20-14321-2020, 2020.
873 Zhang, Y. L., Kang, S. C., Cong, Z. Y., Schmale, J., Sprenger, M., Li, C. L., Yang, W., Gao, T. G.,
874 Sillanpaa, M., Li, X. F., Liu, Y. J., Chen, P. F., and Zhang, X. L.: Light-absorbing impurities enhance
875 glacier albedo reduction in the southeastern Tibetan plateau, *J Geophys Res-Atmos*, 122, 6915-
876 6933, 10.1002/2016jd026397, 2017.
877 Zwaafink, C. D. G., Grythe, H., Skov, H., and Stohl, A.: Substantial contribution of northern high-
878 latitude sources to mineral dust in the Arctic, *Journal of Geophysical Research-Atmospheres*, 121,
879 13678-13697, 10.1002/2016jd025482, 2016.

880

Formatted: Normal

Formatted: Font: (Default) Times New Roman, 小四, Font color: Blue